Multiscale modeling of carbon nanotubes under axial tension and compression

S. H. Yeak and T. Y. Ng
Nanyang Centre for Supercomputing and Visualisation, School of Mechanical and Aerospace Engineering, Nanyang Technological University, 50 Nanyang Avenue, Singapore 639798

K. M. Liew
Department of Building and Construction, City University of Hong Kong, Tat Chee Avenue, Kowloon, Hong Kong
(Received 18 May 2005; revised manuscript received 20 July 2005; published 3 October 2005)

In this paper, we study the elastic and plastic properties of single-walled carbon nanotubes (SWCNTs) under axial compression and tension. The present work employs molecular dynamics (MD) as well as a multiscale technique where a handshaking region between MD and tight-binding (TB) is described and implemented. The interaction forces between the carbon atoms are calculated based on the second-generation reactive empirical bond-order potential, TB derived forces, as well as long-range Lennard-Jones potential. A smooth cutoff Lennard-Jones with switch function is also explored. The detection of sideway buckling due to the asymmetrical axial compression is reported and discussed. This sideway buckling phenomenon is observed when using both pure MD and MD/TB multiscale models. The viability of the presently developed handshaking region between MD and TB in CNTs under axial compression and tension is thus validated.

DOI: 10.1103/PhysRevB.72.165401 PACS number(s): 61.46.+w, 31.15.Qg, 62.20.Mk, 62.25.+g

I. INTRODUCTION

The discovery of multi-walled carbon nanotubes in 1991 by Iijima[1] has stimulated very broad and intense research into the syntheses and theoretical analyses of carbon nanotubes (CNTs) and their applications. This is due to their excellent mechanical properties such as small size, low density, high stiffness, high strength, and excellent electronic properties. Yakobson *et al.*[2] studied CNT behavior under axial compression using the Tersoff-Brenner potential. Their simulations showed that at large deformations, an abrupt release of energy is accompanied by a reversible switch into a different morphological pattern. Yakobson *et al.*[3] also studied CNT behavior under high rate tension using Tersoff-Brenner's reactive empirical bond-order (REBO) potential (see Ref. 4). Their research revealed the ability of CNTs to undergo large elastic deformation when subjected to axial tension. Liew *et al.*[5–7] examined the buckling behavior of single-walled and multi-walled CNTs under axial compression. Their thermal stability analysis showed that single-walled CNTs are thermally more stable than multi-walled CNTs. In addition, they found that critical buckling loads of CNT bundles are much higher than individual single-walled CNT.

The above-mentioned works are based upon empirical molecular dynamics. However, as pointed out by Abraham *et al.*,[8–10] a more refined description is necessary, especially in the bond-breaking area. In other words, potentials due to electron-electron, electron-ion, as well as ion-ion interactions should be considered. In this respect, the tight-binding (TB) method has the advantage of being quantum mechanical where it takes into account the kinetic energies of both the ions and electrons, as well as the electron-electron, electron-ion, and ion-ion interactions.

In the present study, a multiscale model is developed by introducing near and far regions in order to achieve a seamless coupling between MD and TB.

II. COMPUTATIONAL MODEL

In this work, the short-range interaction force between atoms is modeled using the second-generation reactive empirical bond-order (REBO) potential of Brenner *et al.*[4] In addition, the van der Waals potential[11,12] is applied. The potential sum is thus

$$E = \sum_i \sum_{j>i} (E_{ij}^{REBO} + E_{ij}^{vdw}), \tag{1}$$

$$E_{ij}^{REBO} = [V_R(r_{ij}) + b_{ij} V_A(r_{ij})], \tag{2}$$

where V_R and V_A are pair-additive interactions that represent all interatomic repulsion and attraction from the valence electrons, and b_{ij} is the reactive empirical bond order between atoms.

For SWCNTs, the Lennard-Jones 12-6 potential[13] is used

$$E_{ij}^{vdw} = 4\varepsilon \left[\left(\frac{\sigma}{r_{ij}} \right)^{12} - \left(\frac{\sigma}{r_{ij}} \right)^{6} \right]. \tag{3}$$

As pointed out by Mao *et al.*,[11] it is advisable to incorporate the van der Waals potential only if the short-distance potential becomes zero. This is to prevent an artificial reaction barrier from forming due to the steep repulsive wall of the Lennard-Jones 12-6 potential in the short range. If E_{vdw} were activated in the short range as well, the sum effect of $(E_{REBO}+E_{vdw})$ will be erroneously high due to the additional accounting, thus forming the artificial force barrier that restricts unbonded atoms from undergoing chemical reaction.

Theoretically, the above barrier will produce nonsmooth potential energy profiles and interatomic forces, leading to a nonsmooth optimization problem during relaxation. Since the nonsmooth optimization algorithm is very time consuming, it is proposed here to modify the above van der Waals potential such that it behaves smoothly around the cutoff distance, $D_{\max}$. The current work employs the conjugate-

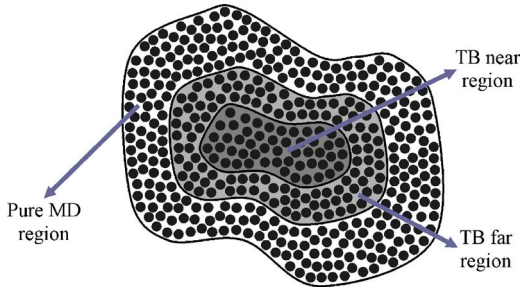

FIG. 1. (Color online) Terminology for regions used in the presently developed multiscale model.

gradient method and truncated-Newton via Lanczos minimization. Both methods are based on smooth objective minimization using the gradient of the objective function.

The original equation will be modified by including a switch function $S(r)$ as shown below,

$$E_{vdw}^{s} = E_{ij}^{vdw} \cdot S(r), \tag{4}$$

which must satisfy the following conditions:

$$E_{vdw}^{s}(D_{\max}) = 0,$$

$$E_{vdw}^{s}(D_{\max} + d) = E_{ij}^{vdw}(D_{\max} + d),$$

$$\left.\frac{\partial}{\partial r} E_{vdw}^{s}\right|_{D_{\max}} = 0,$$

$$\left.\frac{\partial}{\partial r} E_{vdw}^{s}\right|_{D_{\max}+d} = \left.\frac{\partial}{\partial r} E_{ij}^{vdw}\right|_{D_{\max}+d}, \tag{5}$$

where $D_{\max}$ is the distance at which the REBO potential becomes zero, and d is the neighbor distance that causes the switch function to vary from zero to one. The switch function is cubic polynomial and can be calculated by solving Eq. (5) simultaneously. Finally, we derive a smooth cutoff van der Waals potential as

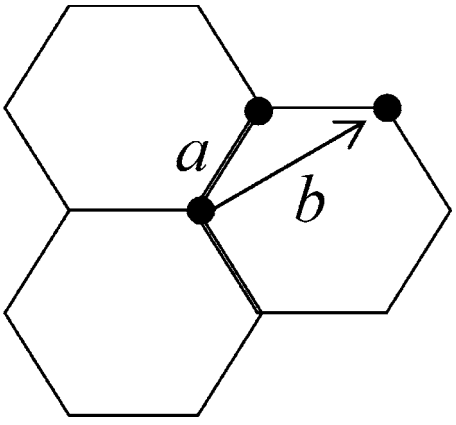

FIG. 2. Nearest distances a and b.

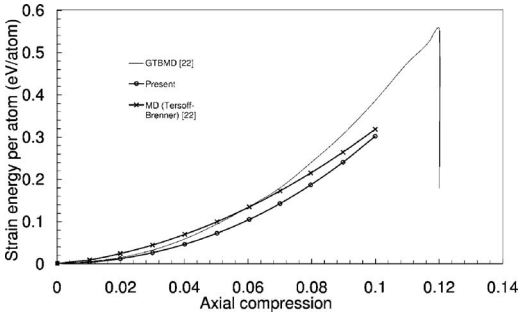

FIG. 3. Comparison of strain energy curve of SWCNT (8,0) under axial compression.

$$E_{vdw} = \begin{cases} 0, & r < D_{\max}, \\ E_{ij}^{vdw} \cdot S(r), & D_{\max} \leqslant r \leqslant D_{\max} + d, \\ E_{ij}^{vdw}, & r > D_{\max} + d. \end{cases} \tag{6}$$

For the quantum mechanical approach, semi-empirical tight-binding (TB) is employed.[14,15] The electronic structure of the simulated CNTs is calculated by a TB Hamiltonian so that the quantum mechanical many-body nature of the interatomic forces is naturally taken into account.

The Hamiltonian of a system of ion cores and valence electrons can be written in the adiabatic approximation as

$$H_{\text{tot}} = T_i + T_e + U_{ee} + U_{ei} + U_{ii}, \tag{7}$$

where T_i, T_e, U_{ee}, U_{ei}, and U_{ii} are respectively the kinetic energies of the ions and electrons, and the potential energies due to electron-electron, electron-ion, and ion-ion interactions. Within the adiabatic one-electron assumption, the many-body electron Hamiltonian can be reduced to that of one electron moving in the average field due to the other valence electrons and ions. The reduced one-electron Hamiltonian H and its nth eigenfunction $|\Psi_n\rangle$ can therefore be written as

$$H|\Psi_n\rangle = \varepsilon_n|\Psi_n\rangle, \tag{8}$$

where ε_n is the energy of the nth single-particle state. The wave functions $|\Psi_n\rangle$ can be approximated by linear combination

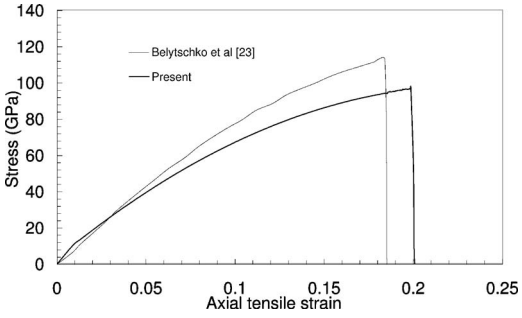

FIG. 4. Comparison of stress-strain curve of a SWCNT (12,12) under axial tension.

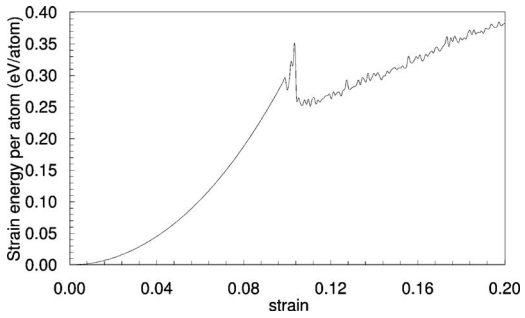

FIG. 5. Strain energy using original Lennard-Jones for SWCNT (8,0) in axial compression.

$$|\Psi_n\rangle = \sum_{l\alpha} c_{l\alpha}^n |\phi_{l\alpha}\rangle, \tag{9}$$

where l is the quantum number index and α labels the ions. The computational load will increase significantly if the basis set, $|\phi_{l\alpha}\rangle$, is not orthogonal. However, it is possible to obtain a new orthogonal basis set $\{\varphi_{l\alpha}\}$ through the Löwdin transform

$$|\Psi_n\rangle = \sum_{l\alpha} b_{l\alpha}^n |\varphi_{l\alpha}\rangle, \tag{10}$$

$$Hb^n = \varepsilon_n b^n, \tag{11}$$

where $b^n = \{b_{l\alpha}^n\}$.

Finally, the Schrödinger equation for the single-particle states becomes

$$\sum_{l'\beta} (\langle \varphi_{l'\beta}|H|\varphi_{l\alpha}\rangle - \varepsilon_n \delta_{ll'}\delta_{\alpha\beta}) c_{l'\beta}^n = 0. \tag{12}$$

In the general approach, the matrix elements in Eq. (12) are calculated after fitting a suitable database obtained either from experiments or by first-principles calculation. Once the single-particle energies are known by solving Eq. (12), the total energy of ion cores and valence electrons can be written as

$$E_{tot} = \sum_n \varepsilon_n f(\varepsilon_n, T) + U_{ii} - U_{ee} = E_{bs} + U_{rep}, \tag{13}$$

where $f(\varepsilon_n, T)$ or the band structure energy, E_{bs}, are the Fermi-Dirac distribution functions. The U_{ee} term corrects the double counting of the electron-electron interactions in the first term. The last two terms constitute the effective repulsive potential, $U_{rep} = U_{ii} - U_{ee}$. This repulsive potential can be expressed as a sum of two-body potentials as

$$U_{rep} = U_{ii} - U_{ee} = \sum_{\alpha,\beta>\alpha} \Phi(r_{\alpha\beta}), \tag{14}$$

where $r_{\alpha\beta}$ is the distance between atoms located at α and β. This pairwise potential $\Phi(r_{\alpha\beta})$ between atoms at α and β can be solved using the transferable TB potential introduced by Xu *et al.*[16]

The forces $f_\alpha(\alpha = 1, 2, \ldots, N_{at})$ that are required in the simulation can be calculated from the Hamiltonian H_{TBMD} as

$$H_{TBMD} = \sum_\alpha \frac{p_\alpha^2}{2m_\alpha} + \sum_n \varepsilon_n f(\varepsilon_n, T) + U_{rep} \tag{15}$$

and the forces are given as

$$f_\alpha = -\sum_n \left\langle \Psi_n \left| \frac{\partial H}{\partial \vec{r}_\alpha} \right| \Psi_n \right\rangle f(\varepsilon_n, T) - \frac{\partial U_{rep}}{\partial \vec{r}_\alpha}. \tag{16}$$

It is found that the second term in Eq. (16) is short ranged and can be solved analytically. The first term, however, is solved using the Hellmann-Feynman theorem

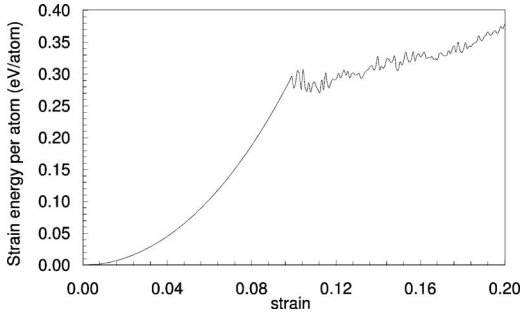

FIG. 6. Strain energy using Lennard-Jones with switch function for SWCNT (8,0) in axial compression.

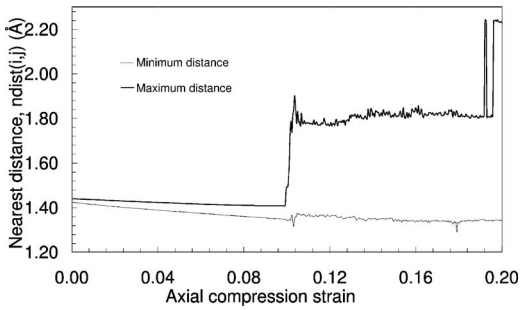

FIG. 7. Nearest distance of SWCNT (8,0) in axial compression using original Lennard-Jones potential.

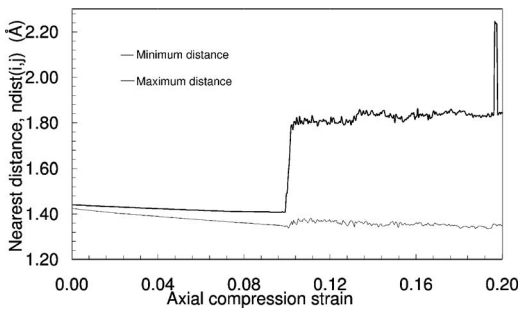

FIG. 8. Nearest distance of SWCNT (8,0) in axial compression using Lennard-Jones with switch function.

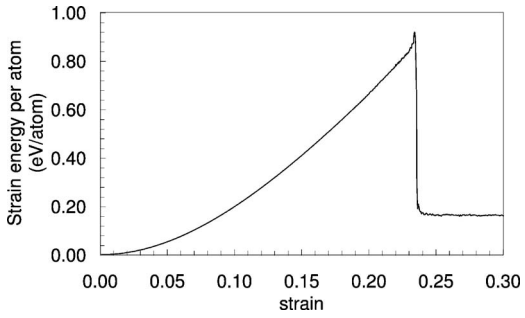

FIG. 9. Strain energy per atom using MD for SWCNT (7,7) under axial tension.

$$\sum_n \left\langle \Psi_n \left| \frac{\partial H}{\partial \bar{r}_\alpha} \right| \Psi_n \right\rangle f(\varepsilon_n, T)$$

$$= -2 \sum_n f(\varepsilon_n, T) \sum_{l\gamma} \sum_{l'\beta} c^n_{l'\beta} \frac{\partial H_{l'\beta,l\gamma}(r_{\beta\gamma})}{\partial \bar{r}_\alpha} c^n_{l\gamma}, \tag{17}$$

where

$$H_{l'\beta,l\gamma}(r_{\beta\gamma}) = g(r_{\beta\gamma}) \langle \varphi_{l'\beta} | H | \varphi_{l\gamma} \rangle |_{r_{\beta\gamma}=r_0} \tag{18}$$

and $g(r_{\beta\gamma})$ is a scaling function. It is important to point out that the Hellmann-Feynman forces require the full set of eigensystem solutions and are therefore very compute intensive.

For the subsequent optimization process, the truncated-Newton method will be effective if only a small number of inner iterations is sufficient to produce a converged step. The implementation of preconditioning will accelerate the convergence of the inner iterations.

The present truncated-Newton method will minimize a twice continuously differentiable function, $f(x)$. The first-order optimality condition leads to

$$\nabla f(x) = 0, \tag{19}$$

$$\nabla^2 f(x_x) p_x = -\nabla f(x_x), \tag{20}$$

$$x_{k+1} = x_k + p_k. \tag{21}$$

The truncated-Newton method is embedded with the following techniques:

conjugate-gradient method to solve large system, Eqs. (20) and (21), iteration is truncated before the exact solution is attained.

line-search method:

for $k=0,1,\ldots$

stop if stopping rule satisfied

compute a search direction p_k

determine an improved estimate, $x_{k+1}=x_k+\alpha_k p_k$.

Trust-region method:

for $k=0,1,\ldots$

stop if stopping rule satisfied

choose p_k so as to minimize $y_k(p) \approx f(x_k+p)$,

subject to $\|p\| \leq \Delta_k$,

compute x_{k+1} and Δ_{k+1} using p_k.

Lanczos shift is used when Hessian matrix, $\nabla^2 f(x)$, is indefinite.

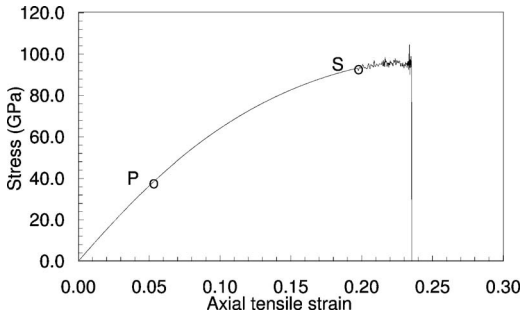

FIG. 10. Stress-strain curve of SWCNT (7,7) under axial tension using MD.

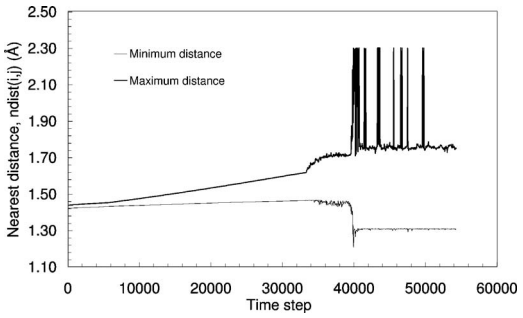

FIG. 11. Nearest distance of SWCNT (7,7) under axial tension using MD.

III. MULTISCALE MODEL

Sherwood[17] demonstrated a successful multiscale approach in the form of a hybrid quantum mechanics/molecular mechanics (QM/MM) model. They introduce outer, boundary, and inner regions in order to achieve seamless coupling. Their subtractive schemes have the advantage of relative simplicity of implementation, with no requirement for validating the QM/MM interactions.

Rafii-Taber *et al.*[18] introduced a multiscale model for simulating brittle-crack propagation. Their model seamlessly couples the crack dynamics at the macroscales and nanoscales via an intermediate mesoscale continuum using a combination of finite elements (FE) and MD. Abraham *et al.*[8,9] studied the rapid brittle fracture of a silicon slab, flawed by a

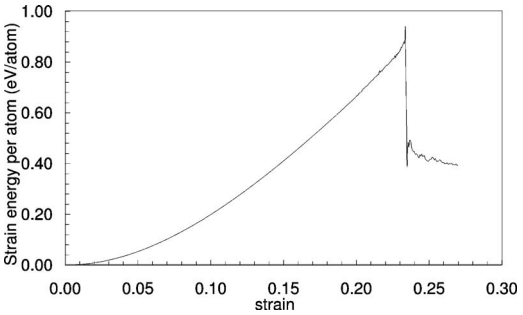

FIG. 12. Strain energy per atom using multiscale method for SWCNT (7,7) under axial tension.

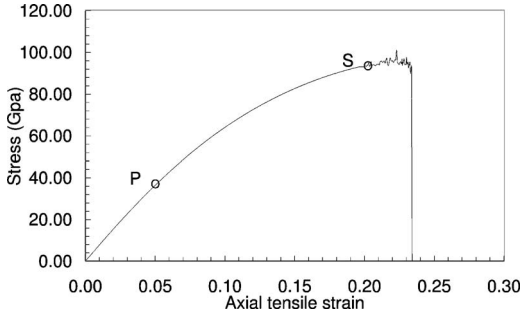

FIG. 13. Stress-strain curve of SWCNT (7,7) under axial tension using multiscale method.

central microcrack and subject to uniaxial tension. They labeled the atomic length scale as the mesoscopic regime, but pointed out that treating bond breaking with an empirical MD potential may be questionable, and a quantum-mechanical treatment is highly desirable.

A multiscale method which successfully couples FE or meshfree methodology with MD was introduced by Dong *et al.*[19] A multiple-scale decomposition of the atomic displacements in terms of FE nodal displacements and MD displacements is first carried out. The total scale is then calculated based on the usual FE interpolation, MD displacements, and the projection of the MD displacements onto the FE basis. Dong *et al.*[20] also introduced a virtual atom cluster (VAC) in the coarse scale treatment, where the number of quadrature points used in the VAC is far less than the actual number of atoms. An "isoparametric-like" meshfree approximation was also formulated and this approximation was found to be valid for interpolating a general class of low-dimensional nanostructured materials such as 2D graphite.

In the presently developed multiscale approach, interpolation scaling is not required. Both the MD and TB methods utilize the information available at the atomic locations. However, unlike the TB method, the MD method does not consider the contributions of valence electrons.

As shown in Fig. 1, the TB domain comprises the near and far regions. The far region constitutes a relatively small subdomain and is used to achieve a seamless coupling between the TB (near region) and MD potentials.

The MD method is applied to both the pure MD and TB far regions. The resultant forces and motions of the atoms in these two regions are therefore determined by the MD method. The TB method is applied to both the TB near and

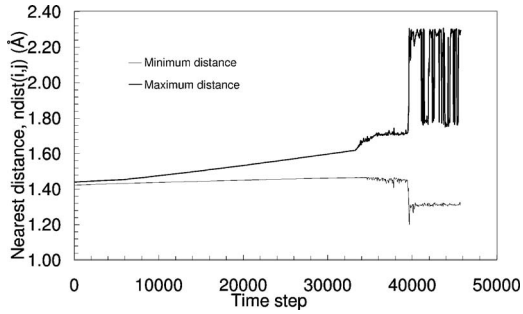

FIG. 14. Nearest distance of SWCNT (7,7) under axial tension using multiscale method.

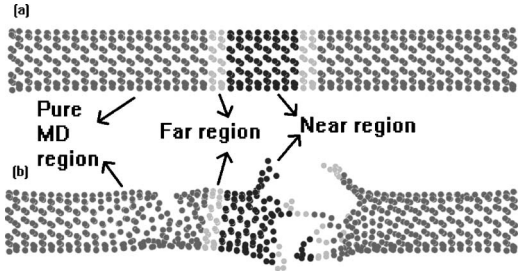

FIG. 15. Multiscale model showing the pure MD, handshaking TB far, and TB near regions in SWCNT: (a) before collapse and (b) after collapse.

far regions but only the motions of the atoms in the near region are determined by the TB method. The model is therefore not affected by the periodic boundary conditions of the TB analysis as the motions of the atoms in the TB far region are based on MD calculations. For the TB analysis of the TB near and far regions, the forces acting on the atoms at the boundary of the TB far region are derived from the MD analysis. The average width of the far region is 2.6 Å since it is the standard cutoff radius of carbon. With the introduction of this far region, the concept of a "silogen atom" is not required in the present model. Silogen is a terminology used by Abraham *et al.*[8,9] to describe TB terminating silicon atoms which bond like silicon but are monovalent like hydrogen.

IV. NEAREST DISTANCE AND DENSITY OF POINT

The nearest mutual distance between two carbon atoms will determine whether their bond is single, double, or if it is broken. Thus, it is useful to calculate the nearest distance among carbon atoms. The nearest distance is indicated as ndist(i,j). The ndist(i,j) table is derived based on the double partial sorting of the entire CNT subject to the constraint of the order $i<j$, where i and j are the indexes of the atoms. The constraint is required to avoid the double counting of each pair of atoms.

Initially in its undeformed state, each atom in the CNT will have three nearest mutual distances, and two for those atoms at the boundary. However, during the simulation, as the CNT deforms, each atom will have at least one nearest mutual distance. From the standard graphene pentagon structure (see Fig. 2), we have

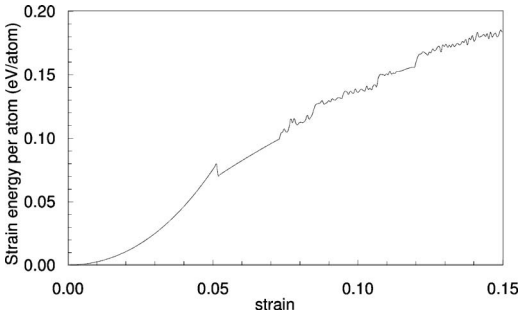

FIG. 16. Strain energy per atom using MD for SWCNT (7,7) under axial compression.

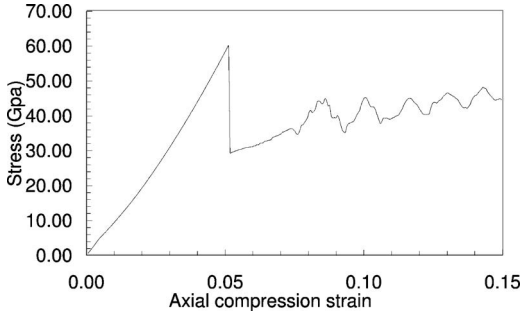

FIG. 17. Stress-strain curve of SWCNT (7,7) under axial compression using MD.

$$b = 2a \cdot \sin(60^\circ) \approx 1.732a. \tag{22}$$

All the distances larger or equal to the designated nearest distance cutoff value of $1.732a$ will be excluded.

The density of point (DOP) is defined here and is calculated so as to detect the buckling, kink shape occurrences as well as bond breaking. All the distances larger than or equal to a designated cutoff distance should be excluded. For instance, if we set the cutoff radius as 2.6 Å, each carbon atom will initially have a DOP value of 9, indicating that it has nine neighboring carbons within the cutoff radius. However, when the SWCNTs start to buckle sideways, it is expected that at the regions of relative larger deformations, some carbon atoms will have DOP values higher than 9. This region will be automatically detected and designated as the near region.

V. SIMULATION RESULTS

In our validation, we apply a velocity of 20 m/s (see Ref. 21) at both ends in order to obtain the stress-strain relationship. The atoms located at the ends of the CNT are moved according to this velocity at very small time steps of 1 femtosecond (fs). In this MD simulation, the locations of the atoms are calculated according to Gear's fifth-order predictor-corrector algorithm. The whole tube was relaxed by truncated-Newton with Lanczos algorithm or by the conjugate-gradient method in order to minimize the energy of CNTs but without affecting the atoms at the two ends.

To validate the presently developed multiscale model, we carry out several comparisons with published data of existing methodologies. Of interest in these comparisons are the Young's modulus and strain energy.

In the microcanonical ensemble molecular dynamics (MD) simulations of CNTs, strain is derived as

$$\varepsilon = |(L - L_0)|/L_0, \tag{23}$$

where L_0 and L are the undeformed and deformed lengths of the CNT. The stress is calculated as

$$\sigma = F/S, \tag{24}$$

where F is axial force and the cross-sectional area is given by $S = \pi dh$, with d being the CNT diameter and h the thickness, which is usually taken to be 0.34 nm.

For the validation, we compare the strain energy of SWCNT (8,0) undergoing axial compression. This comparison is made against results obtained via the quantum GTBMD method, as well as MD results computed with Tersoff-Brenner potential reported by Srivastava[22] in Fig. 3. The reported results show that collapse occurs at the respective strains of 0.12 and 0.8–0.9 for GTBMD and MD (using Tersoff-Brenner potential), whereas the present MD (using second-generation REBO potential) yields a collapse strain of 0.1. The present results are thus in reasonable agreement and are actually more refined than those obtained using the Tersoff-Brenner potential.

Validation of the present MD algorithm is also made for SWCNTs under axial tension. We examine the stress-strain relations of SWCNT (12,12) with length-to-diameter ratio, $L/D = 9.1$. The comparison is made with the MD (using

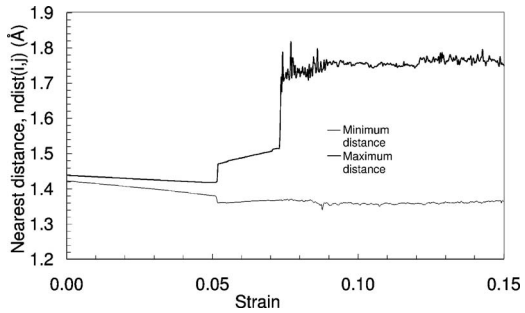

FIG. 18. Nearest distance of SWCNT (7,7) under axial compression using MD.

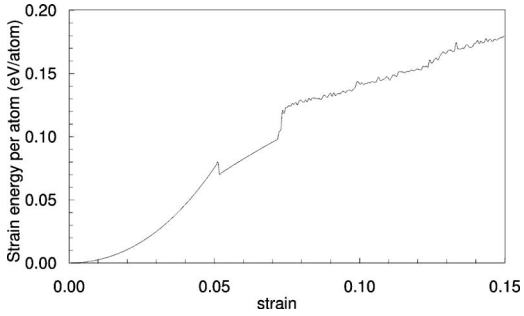

FIG. 19. Strain energy per atom using multiscale method for SWCNT (7,7) under axial compression.

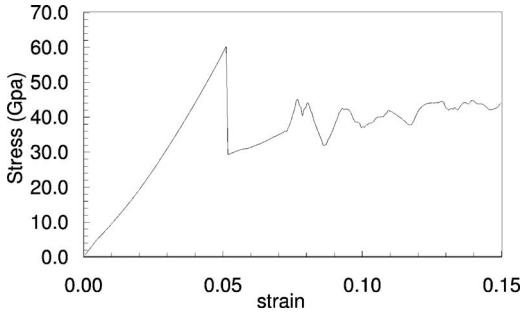

FIG. 20. Stress-strain curve of SWCNT (7,7) under axial compression using multiscale method.

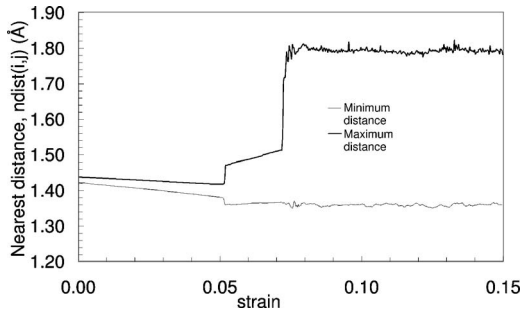

FIG. 21. Nearest distance of SWCNT (7,7) under axial compression using multiscale method.

modified Morse potential) results of Belytschko *et al.*,[23] as shown in Fig. 4. The present results yield a slightly higher collapse strain at a lower stress value.

The third comparison carried out is for the Young's modulus and is made against the *ab initio* results of Kudin *et al.*[24] These results are tabulated in Table I, and it can be observed that the two sets of results are comparable with an average discrepancy of about 5%.

Next we investigate the effects of implementing the switch function into the Lennard-Jones potential. Obviously, the existence of this switch function will not affect the results for a SWCNT under axial tension, where all the atoms are moving away from each other. However, we would expect some differences for the case of axial compression. From Figs. 5–8, we observe that this is indeed the case.

According to Figs. 5–8, we find that both sets of results have the same collapse strain of 0.1. However, we also find that after the initial collapse, results via the smooth cutoff Lennard-Jones show lower strain energy as well as less fluctuation. It is also the same case for maximum distance ndist(i,j) where results using the smooth cutoff Lennard-Jones show less fluctuation in maximum distance. Obviously, this switch function plays important role immediately after the initial collapse.

In order to compare the two presently developed MD and TB/MD schemes, we shall simulate the case of a SWCNT (7,7) with length-to-diameter ratio $L/D=7.1$, and under axial tension.

In this problem, the total number of atoms is 784, with 616 atoms located in the MD region when multiscaling first

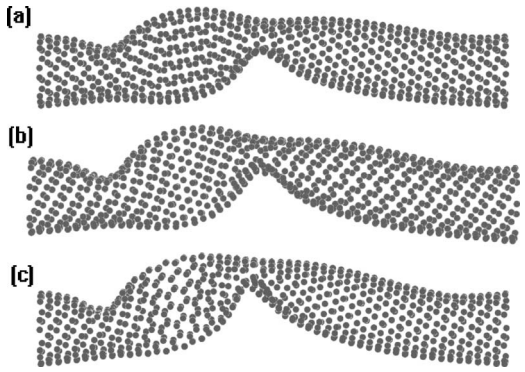

FIG. 22. MD results for sideway buckling at strain values of (a) $\varepsilon=0.0569$, (b) $\varepsilon=0.0683$, and (c) $\varepsilon=0.078$.

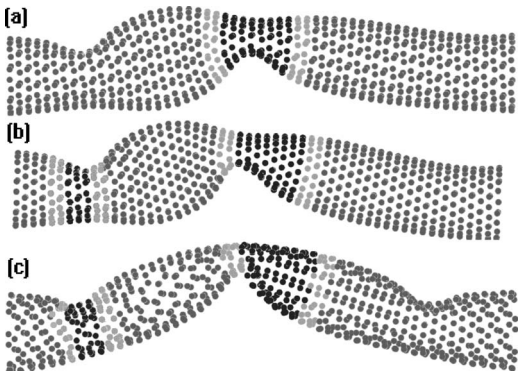

FIG. 23. Multiscale results for sideway buckling at strain values of (a) $\varepsilon=0.0569$, (b) $\varepsilon=0.0683$, and (c) $\varepsilon=0.078$.

occurs. First we perform the pure MD simulation and examine the elastic and plastic behaviors of the SWCNT.

Upon observation of Figs. 9–11, it is found that after the ultimate load point S, the ndist(i,j) tends to converge to two values, namely a minimum value of 1.3 Å and a maximum value of 1.75 Å. The collapse of the SWCNT occurs at the point where a sudden drop in strain energy is observed and at strain $\varepsilon=0.235$. It is interesting to note that the variations of the maximum and minimum ndist(i,j) distances are linear for strain values lower than the ultimate load strain occurring at the point S in the stress-strain curve.

The straight line from the origin to the point P represents the linear elastic region. The points P and S are calculated using the least squares fitting of stress-strain data points. The fitting curves are based on $\sigma=A_p\varepsilon$ and $\sigma=A_s\varepsilon^2+B_s\varepsilon$, respectively, where A_p, A_s, and B_s are the fitting coefficients.

Using the same SWCNT under similar axial tension, we perform the corresponding multiscale model simulation. This multiscale model involves handshaking between MD and TB where 56 atoms are located in the far region and 112 atoms in the near region. Thus, the TB method is used to solve for 168 atoms and this requires the solution of an eigensystem of dimension $672(168\times4)$.

For the multiscale modeling of the axial tension case, the TB near and far regions are implemented, after detecting from initial MD simulations the maximum ndist(i,j) distance exceeding 1.71 Å. From the current comparison of Figs. 9, 10, 12, and 13 it is observed that for both pure MD and multiscale simulations, the SWCNT collapses at strain $\varepsilon=0.235$.

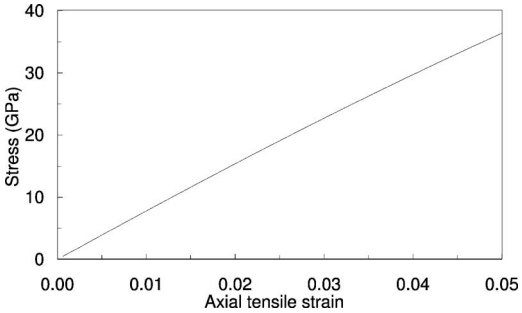

FIG. 24. Smoothness of stress-strain curve when using truncated-Newton minimization.

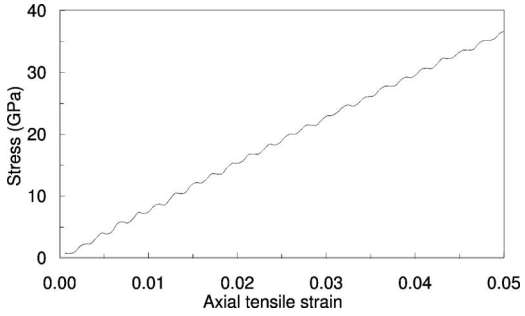

FIG. 25. Smoothness of stress-strain curve when using conjugate-gradient minimization.

From Fig. 14, it is observed that after the ultimate load point S, the minimum and maximum ndist(i,j) distances converge to 1.31 and 1.78 Å, respectively. The above results also show that for the multiscale method, the SWCNT collapses at higher strain energy per atom (0.935 eV/atom) compared with the pure MD case (0.918 eV/atom). Figure 15 depicts the collapse mode of this case study when implementing the multiscale model. As can be observed, the near and handshaking regions are applied only to the critical regions so as to significantly reduce the computational time.

We now move on to compare the numerical results of a SWCNT under axial compression using MD and multiscale TB/MD. In this case study, a SWCNT (7,7) with the length-to-diameter ratio $L/D=7.4$ is used. The total number of carbon atoms is 812, with 644 atoms located in the MD region when multiscaling first occurs. For the first 800 fs of this simulation, we apply a constant velocity of 20 m s^{-1} to the left boundary while the other boundary is applied with a constant velocity of 20 m s^{-1} plus a slight linear velocity increase along the diameter. After 800 fs, all velocities are set to the constant value of 20 m s^{-1}. In the corresponding multiscale simulation, again we initially perform a full MD analysis. The full MD model will shift to at multiscale model after detecting a DOP higher than nine. The present setting acts as the necessary trigger to induce the sideway buckling and avoid the symmetrical modes.

Basically, in the present work, the near and handshaking far TB regions are implemented after detecting a DOP exceeding 9. In this case study, this shift occurs at strain $\varepsilon=0.0518$. Figures 16–18 show the MD results for the variation of the strain energy per atom with strain, the stress-strain curve, and the maximum/minimum ndist(i,j) distances, respectively. The corresponding multiscale results are presented in Figs. 19–21. We observe that the maximum ndist(i,j) distance behaves in a more stable manner for the multiscale model.

TABLE I. Comparison of Young's modulus.

	Young's modulus ($\propto d^2E/d\varepsilon^2$)	
CNT geometry	Present	*ab initio* (Ref. 24)
(4,4)	53.1	56.4
(7,0)	54.6	56.3
(7,7)	52.7	56.5
(12,0)	53.0	55.2

TABLE II. Comparison of computational time.

	Time consumption (s-clock time)	
Strain	Conjugate gradient	Truncated Newton (Ref. 25)
0–0.118	398	463
0.118–0.236	5952	852
0.236–0.32	25716	682

Figures 22 and 23 depict the sideway buckling modes when respectively implementing the MD and multiscale models. Comparing these two figures, we observe that both deformations are very similar at strain values below $\varepsilon=0.072$. However, at strain values higher than $\varepsilon=0.072$, the results from the multiscale model shows more severe deformations.

VI. OPTIMIZATION RESULTS

At present, we employ two minimization schemes, namely, the conjugate-gradient method and the truncated-Newton via the Lanczos algorithm (see Ref. 25). Both schemes are applicable only to smooth solution fields. Theoretically, the truncated-Newton scheme shows superior convergence properties if the starting coordinates are in the vicinity of the solution.

From the simulation results, we observe that both schemes produce quite similar results. However, in terms of computational time, we find that the truncated-Newton method is significantly more efficient.

As can be observed from Table II, the truncated-Newton scheme is relatively more efficient over the entire simulation range. The conjugate-gradient method, on the other hand, is very computationally intensive especially in the bond breaking regime. It is also interesting to note that prior to reaching the yield strain, the conjugate-gradient method is somewhat faster. Finally, we present the smoothness of stress-strain curves when using both the minimization schemes.

From Figs. 24 and 25, we note that the conjugate-gradient method produces results which are somewhat oscillatory (see Fig. 25). Results from the truncated-Newton scheme are significantly smoother.

VII. CONCLUSIONS

In this paper, we have performed a microcanonical ensemble MD as well as developed a novel multiscale model for the study of elastic and plastic deformations of SWCNT under axial compression and tension. Our simulations show that the smoothness of the van der Waals potential is not essential for tensile cases but is important when buckling occurs in axial compression. It was also observed that the nearest distance ndist(i,j) converges to two values for all cases studied, when using both MD and multiscale models.

For relatively low strain values, both MD and multiscale results show high level of correspondence. However, for higher strain values, the results are observed to be fairly distinctive, with the multiscale model exhibiting a relatively lower stiffness. Also, in our simulations, we found that the truncated-Newton via Lanczos minimization performs significantly better than the conjugate gradient method in terms of both the smoothness of the results as well as computational time.

ACKNOWLEDGMENTS

The first author, S. H. Yeak, would like to acknowledge the financial scholarship support from Universiti Teknologi Malaysia.

[1] S. Iijima, Nature (London) **354**, 56 (1991).
[2] B. I. Yakobson, C. J. Brabec, and J. Bernhold, Phys. Rev. Lett. **76**, 2511 (1996).
[3] B. I. Yakobson, M. P. Campbell, C. J. Brabec, and J. Bernholc, Comput. Mater. Sci. **8** 341 (1997).
[4] D. W. Brenner, O. A. Shenderova, J. A. Harrison, S. J. Stuart, Boris Ni, and S. B. Sinnott, J. Phys.: Condens. Matter **14**, 783 (2002).
[5] K. M. Liew, C. H. Wong, X. Q. He, M. J. Tan, and S. A. Meguid, Phys. Rev. B **69**, 115429 (2004).
[6] K. M. Liew, C. H. Wong, X. Q. He, and M. J. Tan, Phys. Rev. B **71**, 075424 (2005).
[7] K. M. Liew, C. H. Wong, and M. J. Tan, Appl. Phys. Lett. **87**, 041901 (2005).
[8] F. F. Abraham, J. Q. Broughton, N. Bernstein, and E. Kaxiras, Europhys. Lett. **44**(6), 783 (1998).
[9] F. F. Abraham, N. Bernstein, J. Q. Broughton, and D. Hess, MRS Bull. **25**, 27 (2000).
[10] C. R. Kmety, J. L. Manson, Q. Huang, J. W. Lynn, R. W. Erwin, J. S. Miller, and A. J. Epstein, Phys. Rev. B **60**, 60 (1999).
[11] Z. Mao, A. Garg, and S. B. Sinnott, Nanotechnology **10**, 273 (1999).
[12] S. B. Sinnott, O. A. Shenderova, C. T. White, and D. W. Brenner, Carbon **36**, 1 (1998).
[13] L. E. Lennard-Jones, Proc. R. Soc. London, Ser. A **106**, 441 (1924).
[14] L. Colombo, Comput. Mater. Sci. **12**, 278 (1998).
[15] L. Colombo and M. Rosati, Comput. Phys. Commun. **128**, 108 (2000).
[16] C. H. Xu, C. Z. Wang, C. T. Chan, and K. M. Ho, "A transferable tight-binding potential for carbon," J. Phys.: Condens. Matter **4**, 6047 (1992).
[17] J. Grotendorst, John von Neumann Institute for Computing, Jülich, NIC Series, Vol. 1, 257–277 (2000).
[18] H. Rafii-Taber, L. Hua, and M. Cross, J. Phys.: Condens. Matter **10**, 2375 (1998).
[19] Q. Dong, G. J. Wagner, and W. K. Liu, Appl. Mech. Rev. **55**(6), 495 (2002).
[20] Q. Dong, G. J. Wagner, and W. K. Liu, Comput. Methods Appl. Mech. Eng. **193**, 1603 (2004).
[21] K. M. Liew, X. Q. He, and C. H. Wong, Acta Mater. **52**, 2521 (2004).
[22] D. Srivastava, M. Menon, and K. Cho, Phys. Rev. Lett. **83**, 2973 (1999).
[23] T. Belytschko, S. P. Xiao, G. C. Schatz, and R. S. Ruoff, Phys. Rev. B **65**, 235430 (2002).
[24] K. N. Kudin and G. E. Scuseria, Phys. Rev. B **64**, 235406 (2001).
[25] S. G. Nash, SIAM (Soc. Ind. Appl. Math.) J. Numer. Anal. **21**(4), 770 (1984).